



# Highly efficient ampere-level CO<sub>2</sub> reduction to multicarbon products via stepwise hollow-fiber penetration electrodes

Xiao Dong<sup>a,1</sup>, Shoujie Li<sup>a,1</sup>, Chang Zhu<sup>a,b,1</sup>, Jianing Mao<sup>a,b</sup>, Gangfeng Wu<sup>a,b</sup>, Guihua Li<sup>a,b</sup>, Guanghui Feng<sup>a,b</sup>, Aohui Chen<sup>a,b</sup>, Yiheng Wei<sup>a,b</sup>, Xiaohu Liu<sup>a,b</sup>, Jiangjiang Wang<sup>a,b</sup>, Yanfang Song<sup>a,b</sup>, Wei Chen<sup>a,b,\*</sup>, Wei Wei<sup>a,b,\*</sup>

<sup>a</sup> CAS Key Laboratory of Low-Carbon Conversion Science and Engineering, Shanghai Advanced Research Institute, Chinese Academy of Sciences, Shanghai 201210, PR China

<sup>b</sup> University of the Chinese Academy of Sciences, Beijing 100049, PR China

## ARTICLE INFO

### Keywords:

Hollow-fiber penetration electrode  
Stepwise CO<sub>2</sub> electroreduction  
Hierarchical porous structure  
Chloride ion regulation

## ABSTRACT

Efficient C<sub>2+</sub> production from CO<sub>2</sub> electrocatalytic reduction exhibits significant promise but suffers from low selectivity and undesired side reactions. Stepwise electroreductions of CO<sub>2</sub> to CO and then to C<sub>2+</sub> products can benefit from the perfect cooperation of the first high CO production efficiency and the subsequent favorable C-C coupling kinetics of CO. Herein, by virtue of serial Ag and Cu hollow-fiber penetration electrodes, a high-efficiency CO<sub>2</sub> electroreduction to C<sub>2+</sub> products is achieved with a partial current density of 1.8 A cm<sup>-2</sup> and a faradaic efficiency of 90.5 %. Experimental results and density functional theory calculations demonstrate that the synergetic combination of unique penetration effect induced by hierarchical micro/nanostructured hollow fiber configurations and regulated electronic structures by chloride ion adsorption, is responsible for the superior activity. This work provides a facile tactic and encouraging headway to design applicable efficient CO<sub>2</sub> electrocatalytic reduction systems towards high-value C<sub>2+</sub> chemicals.

## 1. Introduction

Upgrading carbon dioxide into commodity chemicals and fuels via CO<sub>2</sub> electrocatalytic reduction reaction (CO<sub>2</sub>ERR) has become a promising approach to mitigate CO<sub>2</sub> emissions and store intermittent renewable energy, while the direct synthesis of value-added C<sub>2+</sub> products from CO<sub>2</sub> still suffers from undesired side reactions and relatively low selectivity [1,2]. Using CO instead of CO<sub>2</sub> as feedstock offers a mean to address these challenges, since CO is known as the key reaction intermediate towards C<sub>2+</sub> compounds for CO<sub>2</sub>ERR [1,2], and the electroreduction of CO<sub>2</sub> to CO is much more effective and is being commercially deployed [3,4]. Recent studies of CO electrocatalytic reduction reaction (COERR) have shown that CO can be transformed into C<sub>2+</sub> compounds with high selectivity and reaction rates as well as improved stability, raising the prospect of two-step pathway to transform CO<sub>2</sub> to C<sub>2+</sub> products [3–8].

Furthermore, the sluggish diffusion and limited solubility of CO<sub>2</sub>/CO

(34/0.93 mM at 25 °C and 1 atm) in electrolyte severely restricts CO<sub>2</sub>/COERR and leads to dominant hydrogen evolution reaction (HER) at industrial current density ( $\geq 200$  mA cm<sup>-2</sup>). Gas diffusion electrodes (GDEs) are adopted to accelerate the mass transport at reaction interface via concentration diffusion, allowing efficient CO<sub>2</sub>/COERR towards ampere level [8–17]. Yet, the subtle triphasic interface configurations comprising active catalysts, superhydrophobic polytetrafluoroethylene and conductive carbon, lead to limited performance stability due to mass transfer degradation from flooding and salting out [12–15,18–20], hindering their practical scale-up.

Recently, a kind of self-supported hollow-fiber penetration electrodes (HPEs) with enhanced interface reactions and oriented mass transfer was proposed [21–26]. By forcing CO<sub>2</sub> to disperse and penetrate through the abundant pores on HPE wall, CO<sub>2</sub>ERR kinetics would be greatly boosted due to the subdued mass transfer limitation [26–37]. The unique penetration effect of HPEs improves the CO<sub>2</sub>ERR performance significantly up to ampere level, exhibiting significant potentials

\* Corresponding authors at: CAS Key Laboratory of Low-Carbon Conversion Science and Engineering, Shanghai Advanced Research Institute, Chinese Academy of Sciences, Shanghai 201210, PR China.

E-mail addresses: [chenw@sari.ac.cn](mailto:chenw@sari.ac.cn) (W. Chen), [weiwei@sari.ac.cn](mailto:weiwei@sari.ac.cn) (W. Wei).

<sup>1</sup> These authors contributed equally to this work.

<https://doi.org/10.1016/j.apcatb.2023.122929>

Received 8 March 2023; Received in revised form 8 May 2023; Accepted 28 May 2023

Available online 30 May 2023

0926-3373/© 2023 Elsevier B.V. All rights reserved.

for economically viable CO<sub>2</sub>ERR applications [21–24]. Herein, to further promote the selectivity and current density for C<sub>2+</sub> products simultaneously, we report a highly efficient C<sub>2+</sub> production from stepwise CO<sub>2</sub>ERR over serial Ag and Cu HPEs (Fig. 1), based on synergetic combination of the penetration effect induced by hierarchical structured HPEs and the regulated surface electronic structures by chloride ion (Cl<sup>-</sup>) adsorption. Ampere-level C<sub>2+</sub> productions from stepwise CO<sub>2</sub>ERR were actualized with a partial current density ( $j_{C_{2+}}$ ) of 1.8 A cm<sup>-2</sup> and a faradaic efficiency (FE<sub>C<sub>2+</sub></sub>) of 90.5 %, not only facilitated by the penetration effect of HPEs, but also promoted via favorable CO dimerization from Cl<sup>-</sup>-regulated electronic structures, outperforming those of prominent electrocatalysts.

## 2. Experimental

### 2.1. Preparation of Cl<sup>-</sup> regulated HPEs

In general, both Ag and Cu hollow fibers (HFs) were fabricated by a combined phase-inversion/sintering process from commercial Ag and CuO powders [21–23]. Then the Ag and Cu HPEs with an exposed geometric area of ~ 0.5 cm<sup>2</sup> were obtained by sticking each HF into a copper tube using conductive silver adhesive for electrical contact, while sealing the end of HF and the joint between HF and copper tube with gas-tight and nonconductive epoxy. Both Ag and Cu HPEs were further treated with the electrochemical redox activation/reconstruction to obtain activated Ag and Cu HPEs (noted as aAg HPE and aCu HPE), as well as Cl<sup>-</sup> adsorption regulation via conducting electroreduction in KCl catholyte (noted as Cl-aAg HPE and Cl-aCu HPE). More details can be found in [Supplementary preparation section](#).

### 2.2. Characterization

The cross-section and surface morphologies of HPEs were observed via scanning electron microscopy (SEM) with a SUPRRATM 55 microscope using an accelerating voltage of 5.0 kV. X-ray diffraction (XRD) measurements in the 2θ range from 5° to 90° were performed on a Rigaku Ultima 4 X-ray diffractometer using a Cu Kα radiation source (λ = 1.54056 Å) at 40 kV and 40 mA. X-ray photoelectron spectroscopy (XPS) tests were conducted using a Quantum 2000 Scanning ESCA Microprobe instrument with a monochromatic Al Kα source (1486.6 eV). The binding energies in all XPS spectra were calibrated according to the C 1s peak (284.8 eV). And the XPS spectra were deconvoluted by using Thermo Avantage software after a Shirley background subtraction procedure. The inductively coupled plasma optical emission spectrometry (ICP-OES) tests were performed on a Thermo Fisher iCAP PRO with a 0.02 ppm detection limit for Ag<sup>+</sup> and Cu<sup>2+</sup> using RF Power under 1150 W, a plasma flow of 0.5 L min<sup>-1</sup>, an auxiliary flow of 0.5 L min<sup>-1</sup>, a nebulizer flow of 12.5 L min<sup>-1</sup>, and a sample uptake delay of 30 s. The X-ray absorption fine structure (XAFS) spectroscopy data of Cu K-edge (8979 eV) were collected by a BL14W1 station at 3.5 GeV in transmission mode at the Shanghai Synchrotron Radiation Facility (SSRF) under ambient conditions. The energy was calibrated according to the absorption edge of pure Cu foil, and data was

analyzed in software Athena and Artemis.

### 2.3. Electrochemical measurements

All electrochemical measurements were performed using a Biologic VMP3 potentiostat with a 20 A current booster at ambient temperature and pressure, in a home-made gas-tight two-compartment quartz electrolyzer with a KCl-saturated Ag/AgCl reference electrode, a platinum mesh counter electrode, and a Nafion 117 membrane separator. Both 3.0 M KCl catholyte and 3.0 M KOH anolyte were cycled in respective compartment at a fixed flow rate of 20 mL min<sup>-1</sup>, while CO<sub>2</sub> or CO flow rates were also fixed at 20 mL min<sup>-1</sup>. For long-term performance tests, the current densities were fixed at -2.0 A cm<sup>-2</sup> in 3 M KCl catholyte during entire 200-h tests. The Cl<sup>-</sup> electrochemical adsorption behaviors were determined by performing cyclic voltammetry (CV) tests in 3 M KCl. All current densities in this work were geometrically normalized to the electrode area, while all applied potentials were referred to vs. RHE (reversible hydrogen electrode) with *iR* corrections [38–41]. The error bars of electrocatalytic results were the standard deviation from at least four electrochemical tests for each condition. See more details in [Supplementary electrochemical measurement section](#).

### 2.4. Product quantifications and calculations

Gas-phase products from the cathodic compartment including (CH<sub>4</sub>, CO, C<sub>2</sub>H<sub>4</sub> and H<sub>2</sub>) were directly vented into an online gas chromatograph (GC-2014, Shimadzu, Japan). Liquid-phase products in electrolyte solutions such as MeOH, EtOH and PrOH were offline analyzed using another GC-2014 equipped with a headspace injector, while the formate and acetate were analyzed by a 500 MHz nuclear magnetic resonance (NMR) spectrometer (JNM-ECZ500R, JOEL, Japan). The yields ( $Y_i$ , mol h<sup>-1</sup> cm<sup>-2</sup>) and faradaic efficiencies (FE<sub>*i*</sub>, %) of both gas and liquid products were calculated as  $Y_i = c_i \times v/S$  and  $FE_i = \alpha_i \times c_i \times v \times F \times t / Q \times 100 \%$ , where  $c_i$  (mol L<sup>-1</sup>) is the concentration of gas/liquid products,  $v$  (L h<sup>-1</sup>) is the flow rate of gas reactant/electrolyte,  $S$  (cm<sup>2</sup>) is the geometry electrode area,  $\alpha_i$  is the electrons transfer number for product *i*,  $F$  (96,485 C mol<sup>-1</sup>) is the Faraday constant,  $t$  (h) is the reaction time and  $Q$  (C) is the total charge transferred for electroreduction. By assuming the overpotential of oxygen evolution reaction (OER) on the anode side is zero, the cathodic energy efficiency (EE<sub>*i*</sub>, %) for reduction product was calculated as  $EE_i = (1.23 - E_i) / (1.23 - E) \times FE_i \times 100 \%$ , where  $E$  is the applied potential vs. RHE,  $E_i$  is the thermodynamic potential for obtaining product *i*, and 1.23 (V vs. RHE) is the thermodynamic potential for OER on anode [10–12]. More details can be found in [Supplementary product quantification section](#).

## 3. Results and discussion

Specifically, for stepwise CO<sub>2</sub>ERR, CO<sub>2</sub> is firstly reduced to CO over a Cl<sup>-</sup>-regulated Ag HPE. The Ag HPE was fabricated by a combined phase-inversion/sintering process from commercial Ag powder, followed with electrochemical redox activation (aAg HPE) and further Cl<sup>-</sup> adsorption regulation via conducting electroreduction in KCl catholyte (Cl-aAg HPE).

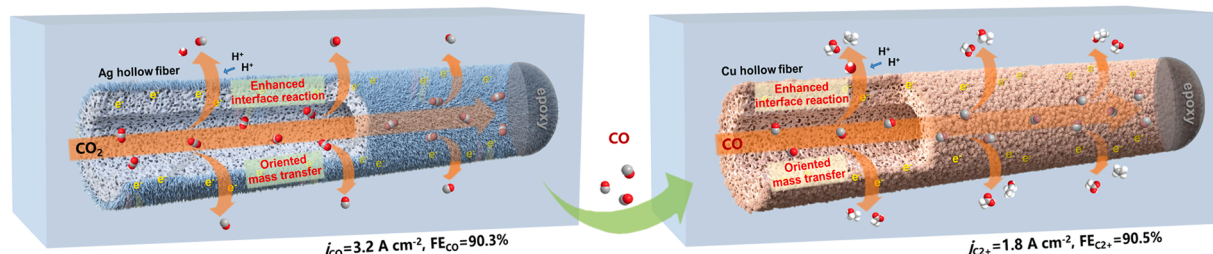


**Fig. 1.** Schematic illustration of the highly efficient stepwise C<sub>2+</sub> production from CO<sub>2</sub>ERR based on serial Ag and Cu hollow-fiber penetration electrodes.

HPE). The slender Ag HPE exhibited a metallic luster (Fig. 2A), and the SEM images showed fused Ag particles rather than spherical Ag powders on Ag HPE surface, as well as abundant interconnected micrometer-sized pores on Ag HPE wall, implying the well-integrated porous substrate of Ag HPE (Fig. S1A–C). Following electrochemical redox activation reconstructed Ag HPE smooth surface into nanorods, configuring hierarchical structured aAg HPE (Fig. S1D–F). Subsequent electroreduction in KCl catholyte (Cl-aAg HPE) preserved the hierarchical porous structures (Fig. 2A and S1G–I), which would facilitate CO<sub>2</sub>ERR with the enlarged reaction interfaces and oriented mass transfer [21,22].

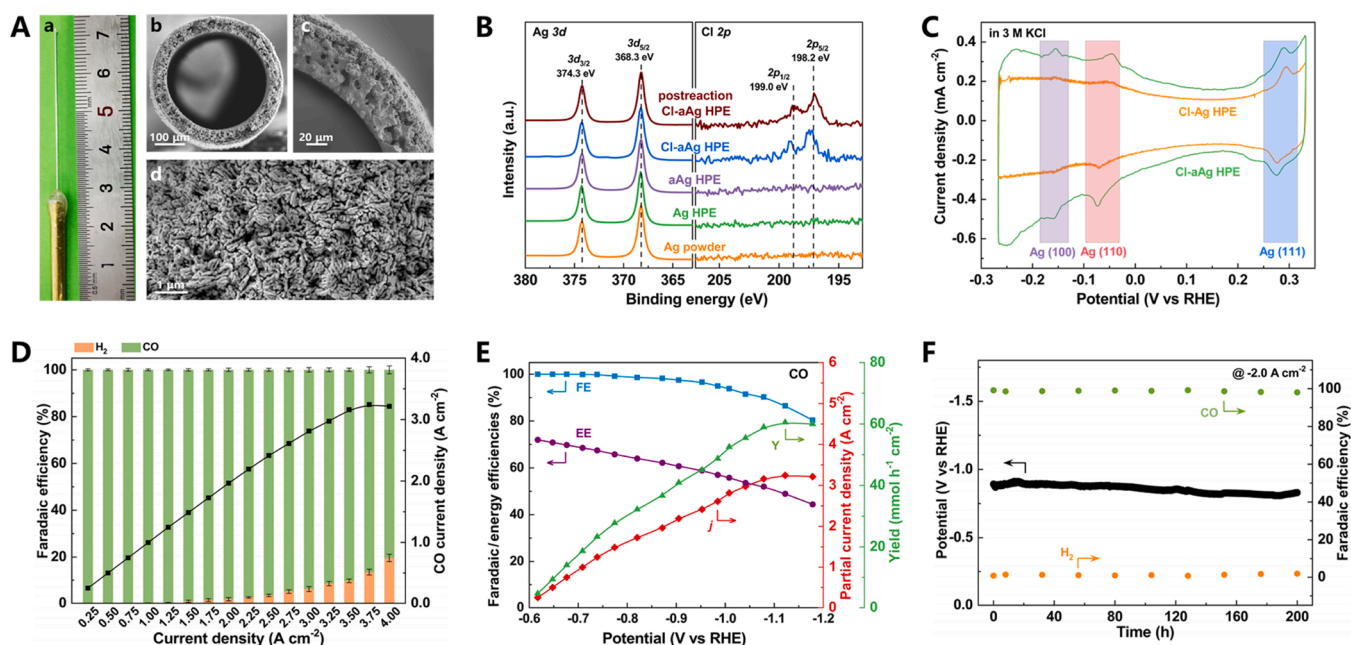
Both XRD (Fig. S2) and XPS (Fig. 2B) of Ag 3d verified that the bulk and surface compositions of Cl-aAg HPE and aAg HPE were identical with metallic Ag [21,22]. While XPS of Cl 2p showed Cl 2p<sub>3/2</sub> and 2p<sub>1/2</sub> peaks on Cl-aAg HPE, which could be indexed to surface adsorbed Cl<sup>−</sup>, while no observable peaks on aAg HPE (Fig. 2B). Besides, reversible Cl<sup>−</sup> adsorption tests conducted via CV measurement revealed the enhanced Cl<sup>−</sup> adsorption over Ag(100) (−0.2 to −0.1 V vs. RHE), (110) (−0.1 to 0 V) and (111) (0.25 to 0.35 V) facets with expanded reaction area for Cl-aAg HPE, comparing with those for Cl-Ag HPE (Fig. 2C and S3). Meanwhile, the relatively strengthened Cl<sup>−</sup> adsorption on Ag(100) and (110) facets, implying an altered surface facet ratio for Cl-aAg HPE [42,43]. These changes originated from the electrochemical redox activation treatment would also benefit the CO production from CO<sub>2</sub>ERR, alongwith the promoted CO<sub>2</sub> activation via Cl<sup>−</sup>-regulated surface electronic structures [22].

Fig. 2D shows the detailed CO<sub>2</sub>ERR performance of Cl-aAg HPE. Only CO and H<sub>2</sub> were detected in the 0.25–4.0 A cm<sup>−2</sup>  $j_{\text{total}}$  range. Particularly, the FE<sub>H<sub>2</sub></sub> remained less than 5 % as the  $j_{\text{total}}$  increased up to 2.75 A cm<sup>−2</sup>, while the FE<sub>CO</sub> remained as high as 90.3 % at the  $j_{\text{total}}$  of 3.5 A cm<sup>−2</sup>, giving a 3.16 A cm<sup>−2</sup>  $j_{\text{CO}}$  at −1.08 V. Corresponding  $Y_{\text{CO}}$  and cathodic EE<sub>CO</sub> over Cl-aAg HPE were 59.0 mmol h<sup>−1</sup> cm<sup>−2</sup> and 52.0 %, respectively (Fig. 2E). Then the FE<sub>CO</sub> dropped to 86.5 % when the  $j_{\text{total}}$  increased to 3.75 A cm<sup>−2</sup>, implying a rising HER at further elevated  $j_{\text{total}}$ . Besides, both FE<sub>CO</sub> and cathodic EE<sub>CO</sub> decreased from 100–80.4 % and 72.0–44.4 %, while  $j_{\text{CO}}$  and  $Y_{\text{CO}}$  increased to the maximums of 3.24 A cm<sup>−2</sup> and 60.5 mmol h<sup>−1</sup> cm<sup>−2</sup>, respectively, with the elevation of  $j_{\text{total}}$  (Fig. 2E). Further durability evaluation of Cl-aAg HPE was performed via a continuous CO<sub>2</sub>ERR test operated at the  $j_{\text{total}}$  of

2.0 A cm<sup>−2</sup> (Fig. 2F). The FE<sub>CO</sub> remained around 98 % with a fluctuating potential between −0.8 and −0.9 V. No sign of decline was observed during the 200-hour test, indicating a durability of 400 A h cm<sup>−2</sup>. Here the durability (A h cm<sup>−2</sup>) considering both working condition (A cm<sup>−2</sup>) and stability (h) was used to indicate the long-term performance, since the capability of working stably at large current density conditions is much critical for practical electrocatalytic systems. Note that the post-reaction XRD and XPS results revealed that the structure and composition of Ag HPE was unchanged after electroreduction (Fig. 2b and S2), and the ICP-OES measurements of the post-reaction electrolytes indicated that no Ag dissolution was occurred (Table S1). Thus the simple single-active-component configuration of HPEs leads to admirable long-term stability, especially at above ampere-level conditions. Such CO<sub>2</sub>ERR to CO performance stands out among recent prominent electrocatalysts (Table S2) [14–17,21,22], which is originated from not only the penetration effect of adequate oriented mass transfer and enhanced interface reactions induced by hierarchical structured HPE [21], but also the heightened CO<sub>2</sub> activation and hindered HER via Cl<sup>−</sup>-regulated surface electronic structures [22], laying good foundations for the subsequent C<sub>2+</sub> production from CO<sub>2</sub>ERR.

Then CO was further electroreduced into C<sub>2+</sub> products over a Cl<sup>−</sup> regulated Cu HPE prepared with similar procedures. The Cu HPE with metallic luster (Fig. 3A) was also fabricated by the phase-inversion/sintering process using commercial CuO powder, followed with in-situ electrochemical reconstruction (aCu HPE) and further Cl<sup>−</sup> regulation via conducting electroreduction in KCl catholyte (Cl-aCu HPE). SEM images of Cu HPE showed finger-like interconnected pores and molten particles rather than spherical CuO powders on Cu HPE (Fig. S4A–C), indicating the well-integrated substrate and abundant micrometer-sized pores. After in-situ electrochemical reconstruction, plentiful globular particles are formed, configuring the hierarchical structured aCu HPE (Fig. S4D–F). No observable structure changes were witnessed during subsequent electroreduction in KCl catholyte, indicating the stable hierarchical porous structure for Cl-aCu HPE (Fig. 3A and S4G–I), which would also greatly facilitate CO<sub>2</sub>ERR by the penetration effect of hierarchical structured HPE with adequate oriented mass transfer and enhanced interface reactions.

Both XRD (Fig. S5), XPS of Cu 2p and Cu LMM Auger spectra



**Fig. 2.** (A) Optical images of Ag HPE and SEM surface/cross section images of Cl-aAg HPE. (B) XPS spectra of Cl 2p and Ag 2p of Ag powder, Ag HPE, aAg HPE, Cl-aAg HPE and postreaction Cl-aAg HPE. (C) Voltammograms of aAg HPE and Cl-aAg HPE. (D) CO<sub>2</sub>ERR performance over Cl-aAg HPE. (E) Faradaic efficiency, and cathodic energy efficiency, partial current density and yield of CO via CO<sub>2</sub>ERR over Cl-aAg HPE. (F) Long-term CO<sub>2</sub>ERR performance at 2.0 A cm<sup>−2</sup> of Cl-aAg HPE.



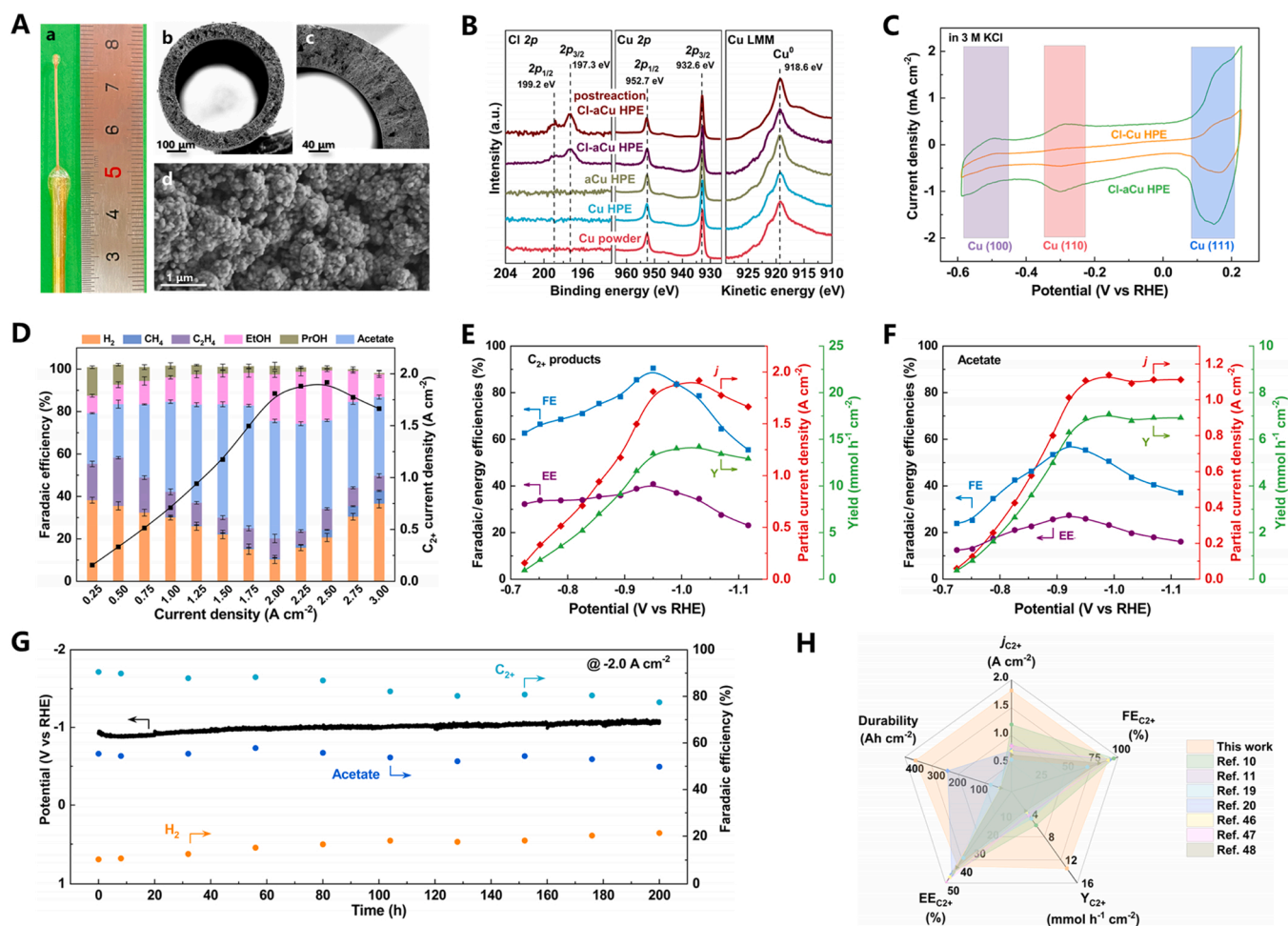


**Fig. 3.** (A) Optical images of Cu HPE and SEM surface/cross section images of Cl-aCu HPE. (B) XPS spectra of Cl 2p, Cu 2p and Cu LMM of Cu powder, Cu HPE, aCu HPE, Cl-aCu HPE and postreaction Cl-aCu HPE. (C) Voltammograms of aCu HPE and Cl-aCu HPE. (D) COERR performance over Cl-aCu HPE. Faradaic efficiency, and cathodic energy efficiency, partial current density and yield of (E)  $\text{C}_{2+}$  products and (F) acetate via COERR over Cl-aCu HPE. (G) Long-term COERR performance of Cl-aCu HPE at  $2.0 \text{ A cm}^{-2}$ . (H) Comparison of Cl-aCu HPE with recent prominent electrocatalysts for  $\text{C}_{2+}$  production from COERR.

(Fig. 3B) verified that the bulk and surface compositions of Cl-aCu HPE and aCu HPE were identical with metallic Cu [23]. Similarly, the surface adsorbed  $\text{Cl}^-$  over Cl-aCu HPE could be observed in XPS spectra of Cl 2p, while no peak on aCu HPE surface (Fig. 3B) [22]. CV curves also exhibited the enhanced reversible  $\text{Cl}^-$  adsorption over Cu(100) ( $-0.55$  to  $-0.45$  V), (110) ( $-0.35$  to  $-0.25$  V) and (111) ( $0.1$  to  $0.2$  V) facets [44,45], as well as expanded reaction area for Cl-aCu HPE, due to the electrochemical reconstruction formed hierarchical structures, comparing with those for Cl-Cu HPE (Fig. 3C and S6) [22,23].

Fig. 3D shows detailed COERR performance over Cl-aCu HPE. Despite the trace amount  $\text{C}_1$  product  $\text{CH}_4$ ,  $\text{C}_{2+}$  products including acetate, ethylene, ethanol and propanol via CO dimerization, as well as  $\text{H}_2$  from competitive HER were obtained at the  $j_{\text{total}}$  range of  $0.25$ – $3.0 \text{ A cm}^{-2}$ . Acetate, which was quantified via nuclear magnetic resonance (NMR) (Fig. S7) dominated in COERR over Cl-aCu HPE at the whole  $j_{\text{total}}$  range. Both the  $\text{FE}_{\text{C}_{2+}}$  and cathodic  $\text{EE}_{\text{C}_{2+}}$  increased from  $62.6\%$  and  $32.3\%$ , reaching peak values of  $90.5\%$  and  $40.8\%$  when the  $j_{\text{total}}$  increased to  $2.0 \text{ A cm}^{-2}$  at  $-0.95$  V (Fig. 3E). Correspondingly, the  $\text{C}_{2+}$  products exhibited a  $j_{\text{C}_{2+}}$  of  $1.8 \text{ A cm}^{-2}$  and a  $Y_{\text{C}_{2+}}$  of  $13.5 \text{ mmol h}^{-1} \text{ cm}^{-2}$ , which greatly surpassed the performance of direct  $\text{CO}_2$ ERR towards  $\text{C}_{2+}$  compounds (Fig. S8). To be specific, the FEs of acetate, ethylene, ethanol and propanol were  $55.4\%$ ,  $9.1\%$ ,  $21.9\%$  and  $4.1\%$ , respectively. Although the  $\text{FE}_{\text{C}_{2+}}$  decreased with the further increase of  $j_{\text{total}}$ , the  $j_{\text{C}_{2+}}$  and  $Y_{\text{C}_{2+}}$  further elevated to the maximums of  $2.0 \text{ A cm}^{-2}$  and  $14.2 \text{ mmol h}^{-1} \text{ cm}^{-2}$  with a  $\text{FE}_{\text{C}_{2+}}$  of  $78.7\%$  at

$-1.03$  V (Fig. 3E). In addition, with the elevation of  $j_{\text{total}}$ , the  $\text{FE}_{\text{acetate}}$  and cathodic  $\text{EE}_{\text{acetate}}$  increased promptly to reach the peak values of  $57.8\%$  and  $25.3\%$  at the  $j_{\text{total}}$  of  $1.75 \text{ A cm}^{-2}$ , giving a  $1.0 \text{ A cm}^{-2}$   $j_{\text{acetate}}$  and a  $9.4 \text{ mmol h}^{-1} \text{ cm}^{-2}$   $Y_{\text{acetate}}$  at  $-0.92$  V. Then plateaus of  $\sim 1.1 \text{ A cm}^{-2}$   $j_{\text{acetate}}$  and  $\sim 10.5 \text{ mmol h}^{-1} \text{ cm}^{-2}$   $Y_{\text{acetate}}$  were maintained at further elevated  $j_{\text{total}}$  range from  $2.0$  to  $3.0 \text{ A cm}^{-2}$  (Fig. 3F). Furthermore, the durability evaluation of Cl-aCu HPE was performed in a continuous COERR operated at the  $j_{\text{total}}$  of  $2.0 \text{ A cm}^{-2}$  (Fig. 3G). The  $\text{FE}_{\text{C}_{2+}}$  gradually went down from  $90\%$  to  $80\%$  in the whole 200-hour test, with fluctuated  $\text{FE}_{\text{acetate}}$  ( $50$ – $60\%$ ) and potential ( $-0.9$  to  $-1.0$  V), indicating a durability of  $400 \text{ A h cm}^{-2}$ . The post-reaction XRD/XPS and ICP-OES results revealed no structure/composition change and dissolution of Cu HPE after electroreduction (Fig. 3b, S5 and Table S1). Such  $\text{C}_{2+}$  products and acetate formation performance from COERR outperform recent prominent electrocatalysts (Fig. 3H, Tables S3 and S4) [10,11,19,20,46–48], which should be attributed to the penetration effect of adequate oriented mass transfer and greatly enlarged triphasic reaction interfaces due to the hierarchical structure formed by electrochemical reconstruction [23].

It is generally accepted that large current densities in water-based electrolytes will lead to the high local pH near the electrode surface, which inhibits the HER and increases  $\text{CO}_2$  reduction due to the proton depletion. But only high local pH is not enough for highly efficient  $\text{CO}_2$ ERR, sufficient reactants supply ( $\text{CO}_2$  and CO in this work) as well as quick removal of corresponding reduction products are far more crucial.

Our previous works [21,23] have proved that the HPE configuration could deliver large and stable CO<sub>2</sub>ERR current density lying in the enhanced three-phase interface reactions and mass transfers. This is also applicable for COERR. As shown in Fig S9, the COERR over aCu HPE in 3.0 M KOH could also give an ampere-level  $j_{C_2+}$  with a FE<sub>C<sub>2</sub>+</sub> of 66.8 % by virtue of the hierarchical structured HPE. Additionally, the regulated electronic structures by chloride ion adsorption of Cl-aCu HPE in 3.0 M KCl further promote the  $j_{C_2+}$  and FE<sub>C<sub>2</sub>+</sub> towards 1.8 A cm<sup>-2</sup> and 90.5 %, which clearly showed the functions of Cl<sup>-</sup> regulation on the promotion of C-C coupling and the suppression of HER.

Thus, XAFS spectroscopy including X-ray absorption near-edge structure (XANES) and extended X-ray absorption fine structure (EXAFS) of Cl-aCu HPE were intensively investigated to explore the coordination environments of Cu species in Cu HPEs for revealing the intrinsic characteristics of chloride ion adsorption. Both the XANES spectra and the  $k^3$ -weighted  $\chi(k)$  function of EXAFS Fourier transform spectra for aCu HPE and Cl-aCu HPE were similar to reference Cu foil (Fig. 4A–B), exhibiting metallic Cu features, which is consistent with XRD and XPS results. Interestingly, further fitting results (Fig. 4B–C and Table S5) showed, for Cl-aCu HPE, besides the dominant peak at 2.56 Å of characteristic Cu-Cu coordination, a weak peak at 1.93 Å implied a Cu-Cl coordination with a low coordination number of 0.9 which originated from chloride ion adsorption [9]. In contrary, reference CuCl<sub>2</sub> possessed a peak at 2.35 Å of the typical Cu-Cl scattering path with a coordination number of 4 from bonding between Cu and Cl atoms [49]. Besides, the Cu-Cl scattering path in CuCl also exhibiting a peak around 2.3 Å with a coordination number of 3 [49]. These distinctions suggested the low-coordination state of the trace chloride ion adsorption species on Cl-aCu HPE surface [9,50].

Moreover, detailed density functional theoretical (DFT) calculations were further conducted to obtain more insights of Cl<sup>-</sup> regulation effect on the energetics of both C-C coupling in COERR and competitive HER over Cu(111) facet with and without Cl<sup>-</sup> (Figs. S10–S12). Fig. 4D–E shows the free energy diagrams of the dimerization of \*CO to form \*COCO and following \*COHCOH, as well as the subsequent

dehydration to form \*CCO and \*H towards acetate and ethylene, respectively [6,7,51,52]. The reaction free energies for forming \*COCO intermediate via C-C coupling of two \*CO with H<sup>+</sup> and e<sup>-</sup> on Cu(111) and Cl-Cu(111) ramped up from -1.08 to 0.35 eV and -1.10 to 0.22 eV, respectively. Then free energies for further hydrogenation towards \*COHCOH went down to 0.18 eV on Cu(111) and 0.01 eV on Cl-Cu(111). In contrast, the free energies for forming \*H was 0.04 eV on Cl-Cu(111), higher than that of -0.07 eV on bare Cu(111). Thus, the Cl<sup>-</sup> adsorption on Cu(111) surface decreases the energy barrier for CO dimerization, and increases the HER barrier, indicating the more favorable pathway to generate \*COCO and \*COHCOH, rather than \*H. Besides, free energies for subsequent dehydration towards \*CCO and \*CCOH on Cu(111) and Cl-Cu(111) surfaces showed significant distinction. For \*CCO formed from \*COHCOH direct dehydration, considered to be intermediate toward acetate [51,52], the free energies went down to -0.83 and -0.84 eV on Cu(111) and Cl-Cu(111). While for \*CCOH from the dehydration of \*COHCOH with additional H<sup>+</sup> and e<sup>-</sup>, as the key intermediate toward ethylene [51,52], the free energies went up to 0.24 and 0.03 eV on Cu(111) and Cl-Cu(111). These indicated that acetate are more prone to be formed in COERR [10,19,20]. Consequently, the DFT results verified that the adsorbed Cl<sup>-</sup> on Cu facets not only promoted the COERR activity via suppressing competitive HER, but also the simultaneously enhanced the C-C coupling of CO towards C<sub>2</sub>+ products.

#### 4. Conclusion

In summary, a stepwise CO<sub>2</sub>ERR strategy using Ag and Cu HPEs was adopted to reach high-rate C<sub>2</sub>+ production. CO<sub>2</sub> was firstly reduced into CO over a Cl<sup>-</sup> regulated Ag HPE with a 3.2 A cm<sup>-2</sup>  $j_{CO}$  and a 90.3 % FE<sub>CO</sub>, and then a Cl<sup>-</sup> regulated Cu HPE further converted CO into C<sub>2</sub>+ products with a 1.8 A cm<sup>-2</sup>  $j_{C_2+}$  and a 90.5 % FE<sub>C<sub>2</sub>+</sub>. The optimal current density range was from 2 to 2.5 A cm<sup>-2</sup>, to reach considerable selectivity, energy efficiency and stability at industry-level current density at the same time feasibly. The synergetic combination of the unique penetration

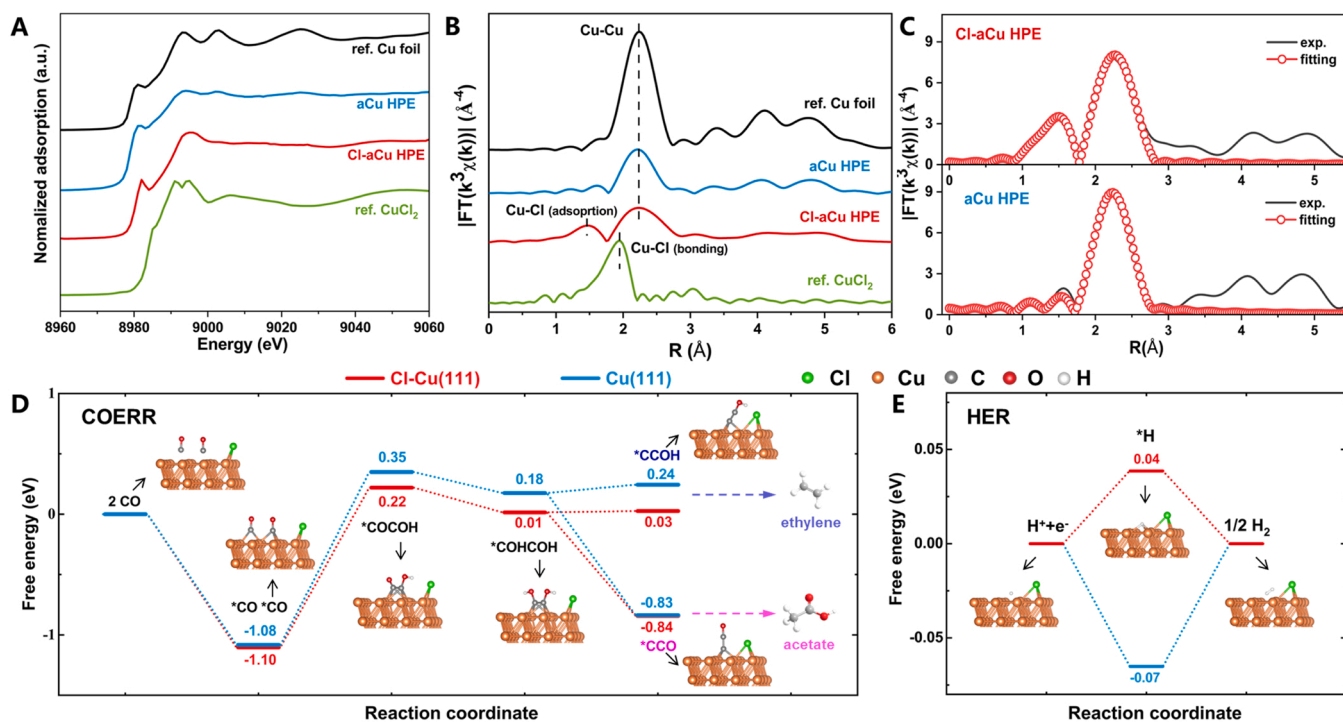


**Fig. 4.** (A) Normalized XANES spectra and (B) Fourier transform of EXAFS data of reference Cu foil, Cu HPE, Cl-Cu HPE and reference CuCl<sub>2</sub> samples at the Cu K-edge. (C) The fitting for the EXAFS data of Cu HPE and Cl-Cu HPE. Calculated Gibbs free energy diagrams for (D) COERR and (E) HER over Cu(111) (blue) and Cl-Cu(111) (red), respectively.

effect and the regulated electronic structures resulted in the striking high-rate CO<sub>2</sub>ERR performance toward C<sub>2+</sub> production. This work provides a facile tactic and inspiration to design electrocatalytic systems with exceedingly efficient CO<sub>2</sub>ERR of high current density and selectivity as well as good durability, presenting an encouraging headway of the scalable CO<sub>2</sub>ERR applications towards high-value C<sub>2+</sub> chemicals.

### CRedit authorship contribution statement

**Xiao Dong:** Experiments, Data curation, Writing – original draft. **Shoujie Li:** Experiments, Data curation, Writing – review & editing. **Chang Zhu:** Experiments, Data curation, Writing – review & editing. **Jianing Mao:** Experiments, Data curation. **Gangfeng Wu:** Data curation. **Guihua Li:** Data curation. **Guanghui Feng:** Data curation. **Aohui Chen:** Data curation. **Yiheng Wei:** Data curation. **Xiaohu Liu:** Data curation. **Jiangjiang Wang:** Data curation. **Yanfang Song:** Data curation. **Wei Chen:** Conceptualization, Data curation, Writing – review & editing, Supervision. **Wei Wei:** Supervision.

### Declaration of Competing Interest

The authors declare no conflict of interest.

### Data Availability

Data will be made available on request.

### Acknowledgements

This work was financially supported by the Ministry of Science and Technology of China (National Key R&D Program of China, 2022YFA1504604); the Strategic Priority Research Program of the Chinese Academy of Sciences, “Transformational Technologies for Clean Energy and Demonstration” (No. XDA 21000000); the Major Project of the Science and Technology Department of Inner Mongolia (No. 2021ZD0020); the Youth Innovation Promotion Association of the Chinese Academy of Sciences (No. E224301401); Shanghai Excellent Principal Investigator (No. 23XD1404400); Shanghai Sailing Program (Nos. 23YF1453300, 18YF1425700); Shanghai Pujiang Program (No. 20PJ1415200); the Outstanding Young Talent Project of Shanghai Advanced Research Institute, the Chinese Academy of Sciences (No. E254991ZZ1); the Foundation of Key Laboratory of Low-Carbon Conversion Science & Engineering, Shanghai Advanced Research Institute, Chinese Academy of Sciences (No. KLLCCSE-202207Z, SARI, CAS). The authors appreciate the BL14W1 beamline of Shanghai Synchrotron Radiation Facility (SSRF), Shanghai, China.

### Appendix A. Supporting information

Supplementary data associated with this article can be found in the online version at [doi:10.1016/j.apcatb.2023.122929](https://doi.org/10.1016/j.apcatb.2023.122929).

### References

- [1] S. Nitopi, E. Bertheussen, S.B. Scott, X. Liu, A.K. Engstfeld, S. Horch, B. Seger, I.E. L. Stephens, K. Chan, C. Hahn, J.K. Nørskov, T.F. Jaramillo, I. Chorkendorff, Progress and perspectives of electrochemical CO<sub>2</sub> reduction on copper in aqueous electrolyte, *Chem. Rev.* 119 (2019) 7610–7672, <https://doi.org/10.1021/acs.chemrev.8b00705>.
- [2] E.W. Lees, B.A.W. Mowbray, F.G.L. Parlange, C.P. Berlinguette, Gas diffusion electrodes and membranes for CO<sub>2</sub> reduction electrolyzers, *Nat. Rev. Mater.* 7 (2021) 55–64, <https://doi.org/10.1038/s41578-021-00356-2>.
- [3] S. Yu, S. Louisa, P. Yang, The interactive dynamics of nanocatalyst structure and microenvironment during electrochemical CO<sub>2</sub> conversion, *JACS Au* 2 (2022) 562–572, <https://doi.org/10.1021/jacsau.1c00562>.
- [4] B. Cao, F.-Z. Li, J. Gu, Designing Cu-based tandem catalysts for CO<sub>2</sub> electroreduction based on mass transport of CO intermediate, *ACS Catal.* 12 (2022) 9735–9752, <https://doi.org/10.1021/acscatal.2c02579>.
- [5] M. Jouny, G.S. Hutchings, F. Jiao, Carbon monoxide electroreduction as an emerging platform for carbon utilization, *Nat. Catal.* 2 (2019) 1062–1070, <https://doi.org/10.1038/s41929-019-0388-2>.
- [6] H. Zhang, J. Li, M.-J. Cheng, Q. Lu, CO electroreduction: current development and understanding of Cu-based catalysts, *ACS Catal.* 9 (2019) 49–65, <https://doi.org/10.1021/acscatal.8b03780>.
- [7] Y. Ji, A. Guan, G. Zheng, Copper-based catalysts for electrochemical carbon monoxide reduction, *Cell Rep. Phys. Sci.* 3 (2022), <https://doi.org/10.1016/j.xcrp.2022.101072>.
- [8] H. Rabiee, L. Ge, X. Zhang, S. Hu, M. Li, Z. Yuan, Gas diffusion electrodes (GDEs) for electrochemical reduction of carbon dioxide, carbon monoxide, and dinitrogen to value-added products: a review, *Energy Environ. Sci.* 14 (2021) 1959–2008, <https://doi.org/10.1039/d0ee03756g>.
- [9] W. Ma, S. Xie, T. Liu, Q. Fan, J. Ye, F. Sun, Z. Jiang, Q. Zhang, J. Cheng, Y. Wang, Electrocatalytic reduction of CO<sub>2</sub> to ethylene and ethanol through hydrogen-assisted C-C coupling over fluorine-modified copper, *Nat. Catal.* 3 (2020) 478–487, <https://doi.org/10.1038/s41929-020-0450-0>.
- [10] J. Li, Z. Wang, C. McCallum, Y. Xu, F. Li, Y. Wang, C.M. Gabardo, C.-T. Dinh, T.-T. Zhuang, L. Wang, J.Y. Howe, Y. Ren, E.H. Sargent, D. Sinton, Constraining CO coverage on copper promotes high-efficiency ethylene electroproduction, *Nat. Catal.* 2 (2019) 1124–1131, <https://doi.org/10.1038/s41929-019-0380-x>.
- [11] M. Jouny, W. Luc, F. Jiao, High-rate electroreduction of carbon monoxide to multicarbon products, *Nat. Catal.* 1 (2018) 748–755, <https://doi.org/10.1038/s41929-018-0133-2>.
- [12] F.P. Garcia de Arquer, C.T. Dinh, A. Ozden, J. Wicks, C. McCallum, A.R. Kirmani, D.H. Nam, C. Gabardo, A. Seifitokaldani, X. Wang, Y.C. Li, F. Li, J. Edwards, L. J. Richter, S.J. Thorpe, D. Sinton, E.H. Sargent, CO<sub>2</sub> electrolysis to multicarbon products at activities greater than 1 A cm<sup>-2</sup>, *Science* 367 (2020) 661–666, <https://doi.org/10.1126/science.aay4217>.
- [13] A. Inoue, T. Harada, S. Nakanishi, K. Kamiya, Ultra-high-rate CO<sub>2</sub> reduction reactions to multicarbon products with a current density of 1.7 A cm<sup>-2</sup> in neutral electrolytes, *EES Catal.* 1 (2023) 9–16, <https://doi.org/10.1039/D2EY00035K>.
- [14] M. Fang, L. Xu, H. Zhang, Y. Zhu, W.-Y. Wong, Metalloporphyrin-linked mercurated graphynes for ultrastable CO<sub>2</sub> electroreduction to CO with nearly 100 % selectivity at a current density of 1.2 A cm<sup>-2</sup>, *J. Am. Chem. Soc.* 144 (2022) 15143–15154, <https://doi.org/10.1021/jacs.2c05059>.
- [15] J.-R. Huang, X.-F. Qiu, Z.-H. Zhao, H.-L. Zhu, Y.-C. Liu, W. Shi, P.-Q. Liao, X.-M. Chen, Single-product faradaic efficiency for electrocatalytic of CO<sub>2</sub> to CO at current density larger than 1.2 A cm<sup>-2</sup> in neutral aqueous solution by a single-atom nanozyme, *Angew. Chem. Int. Ed.* 61 (2022), e202210985, <https://doi.org/10.1002/anie.202210985>.
- [16] S. Li, S. Zhao, X. Lu, M. Ceccato, X.-M. Hu, A. Roldan, J. Catalano, M. Liu, T. Skrydstrup, K. Daasbjerg, Low-valence Zn<sup>0</sup> (0 < δ < 2) single-atom material as highly efficient electrocatalyst for CO<sub>2</sub> reduction, *Angew. Chem. Int. Ed.* 60 (2021) 22826–22832, <https://doi.org/10.1002/anie.202107550>.
- [17] G. Wen, B. Ren, X. Wang, D. Luo, H. Dou, Y. Zheng, R. Gao, J. Gostick, A. Yu, Z. Chen, Continuous CO<sub>2</sub> electrolysis using a CO<sub>2</sub> exsolution-induced flow cell, *Nat. Energy* 7 (2022) 978–988, <https://doi.org/10.1038/s41560-022-01130-6>.
- [18] A. Ozden, J. Li, S. Kandambeth, X.-Y. Li, S. Liu, O. Shekhar, P. Ou, Y. Zou Finck, Y.-K. Wang, T. Alkayyali, F. Pelayo Garcia de Arquer, V.S. Kale, P.M. Bhatt, A.H. Ip, M. Eddaoudi, E.H. Sargent, D. Sinton, Energy- and carbon-efficient CO<sub>2</sub>/CO electrolysis to multicarbon products via asymmetric ion migration-adsorption, *Nat. Energy* 8 (2023) 179–190, <https://doi.org/10.1038/s41560-022-01188-2>.
- [19] M. Luo, A. Ozden, Z. Wang, F. Li, J. Erick Huang, S.-F. Hung, Y. Wang, J. Li, D.-H. Nam, Y.C. Li, Y. Xu, R. Lu, S. Zhang, Y. Lum, Y. Ren, L. Fan, F. Wang, H.-h Li, D. Appadoo, C.-T. Dinh, Y. Liu, B. Chen, J. Wicks, H. Chen, D. Sinton, E.H. Sargent, Coordination polymer electrocatalysts enable efficient CO-to-acetate conversion, *Adv. Mater.* 35 (2023) 2209567, <https://doi.org/10.1002/adma.202209567>.
- [20] Y. Ji, Z. Chen, R. Wei, C. Yang, Y. Wang, J. Xu, H. Zhang, A. Guan, J. Chen, T.-K. Sham, J. Luo, Y. Yang, X. Xu, G. Zheng, Selective CO-to-acetate electroreduction via intermediate adsorption tuning on ordered Cu-Pd sites, *Nat. Catal.* 5 (2022) 251–258, <https://doi.org/10.1038/s41929-022-00757-8>.
- [21] S. Li, W. Chen, X. Dong, C. Zhu, A. Chen, Y. Song, G. Li, W. Wei, Y. Sun, Hierarchical micro/nanostructured silver hollow fiber boosts electroreduction of carbon dioxide, *Nat. Commun.* 13 (2022) 3080, <https://doi.org/10.1038/s41467-022-30733-6>.
- [22] S. Li, X. Dong, Y. Zhao, J. Mao, W. Chen, A. Chen, Y. Song, G. Li, Z. Jiang, W. Wei, Y. Sun, Chloride ion adsorption enables ampere-level CO<sub>2</sub> electroreduction over silver hollow fiber, *Angew. Chem. Int. Ed.* 61 (2022), e202210432, <https://doi.org/10.1002/anie.202210432>.
- [23] C. Zhu, Y. Song, X. Dong, G. Li, A. Chen, W. Chen, G. Wu, S. Li, W. Wei, Y. Sun, Ampere-level CO<sub>2</sub> reduction to multicarbon products over a copper gas penetration electrode, *Energy Environ. Sci.* 15 (2022) 5391–5404, <https://doi.org/10.1039/D2EE02121H>.
- [24] Y. Song, X. Dong, W. Chen, W. Wei, Hollow-fiber gas penetration electrodes efficiently produce renewable synthetic fuels, *Front. Energy* 16 (2022) 700–705, <https://doi.org/10.1007/s11708-022-0842-8>.
- [25] H. Rabiee, J.K. Heffernan, L. Ge, X. Zhang, P. Yan, E. Marcellin, S. Hu, Z. Zhu, H. Wang, Z. Yuan, Tuning flow-through Cu-based hollow fiber gas-diffusion electrode for high-efficiency carbon monoxide (CO) electroreduction to C<sub>2+</sub> products, *Appl. Catal. B-Environ.* (2023), <https://doi.org/10.1016/j.apcatb.2023.122589>.
- [26] R. Kas, K.K. Hummadi, R. Kortlever, P. de Wit, A. Milbrat, M.W.J. Luiten-Olieman, N.E. Benes, M.T.M. Koper, G. Mul, Three-dimensional porous hollow fibre copper electrodes for efficient and high-rate electrochemical carbon dioxide reduction, *Nat. Commun.* 7 (2016) 10748–10754, <https://doi.org/10.1038/ncomms10748>.



- [27] H. Rabiee, L. Ge, X. Zhang, S. Hu, M. Li, S. Smart, Z. Zhu, Z. Yuan, Shape-tuned electrodeposition of bismuth-based nanosheets on flow-through hollow fiber gas diffusion electrode for high-efficiency CO<sub>2</sub> reduction to formate, *Appl. Catal. B-Environ.* 286 (2021) 119945–119956, <https://doi.org/10.1016/j.apcatb.2021.119945>.
- [28] H. Rabiee, L. Ge, X. Zhang, S. Hu, M. Li, S. Smart, Z. Zhu, H. Wang, Z. Yuan, Stand-alone asymmetric hollow fiber gas-diffusion electrodes with distinguished bronze phases for high-efficiency CO<sub>2</sub> electrochemical reduction, *Appl. Catal. B-Environ.* 298 (2021) 120538–120548, <https://doi.org/10.1016/j.apcatb.2021.120538>.
- [29] D. Liu, Y. Hu, E. Shoko, H. Yu, T.T. Isimjan, X. Yang, High selectivity of CO<sub>2</sub> conversion to formate by porous copper hollow fiber: microstructure and pressure effects, *Electrochim. Acta* 365 (2021) 137343–137350, <https://doi.org/10.1016/j.electacta.2020.137343>.
- [30] K.K. Hummadi, A. Sustronk, R. Kas, N. Benes, G. Mul, Optimizing temperature treatment of copper hollow fibers for the electrochemical reduction of CO<sub>2</sub> to CO, *Catalysts* 11 (2021) 571–583, <https://doi.org/10.3390/catal11050571>.
- [31] H. Rabiee, X. Zhang, L. Ge, S. Hu, M. Li, S. Smart, Z. Zhu, Z. Yuan, Tuning the product selectivity of the Cu hollow fiber gas diffusion electrode for efficient CO<sub>2</sub> reduction to formate by controlled surface Sn electrodeposition, *ACS Appl. Mater. Interfaces* 12 (2020) 21670–21681, <https://doi.org/10.1021/acsami.0c03681>.
- [32] B. Chen, J. Xu, J. Zou, D. Liu, Y. Situ, H. Huang, Formate-selective CO<sub>2</sub> electrochemical reduction with a hydrogen-reduction-suppressing bronze alloy hollow-fiber electrode, *ChemSusChem* 13 (2020) 6594–6601, <https://doi.org/10.1002/cssc.202002314>.
- [33] C. Zhu, G. Shen, W. Chen, X. Dong, G. Li, Y. Song, W. Wei, Y. Sun, Copper hollow fiber electrode for efficient CO<sub>2</sub> electroreduction, *J. Power Sources* 495 (2021) 229814–229820, <https://doi.org/10.1016/j.jpowsour.2021.229814>.
- [34] X. Dong, G. Li, W. Chen, C. Zhu, T. Li, Y. Song, N. Sun, W. Wei, Gas-phase CO<sub>2</sub> electroreduction over Sn-Cu hollow fibers, *Mater. Adv.* 2 (2021) 241–247, <https://doi.org/10.1039/d0ma00851f>.
- [35] X. Dong, G. Li, W. Chen, C. Zhu, Y. Song, N. Sun, W. Wei, Ag modified Cu hollow fiber for gas-phase CO<sub>2</sub> electrocatalytic conversion to oxygenates, *Chin. Sci. Bull.* 66 (2020) 816–824, <https://doi.org/10.1360/tb-2020-0512>.
- [36] S. Li, X. Dong, W. Chen, Y. Song, G. Li, W. Wei, Y. Sun, Efficient CO<sub>2</sub> electroreduction over silver hollow fiber electrode, *Catalysts* 12 (2022) 453.
- [37] G. Li, Y. Song, C. Zhu, X. Dong, W. Chen, G. Wu, G. Feng, S. Li, W. Wei, Facet-oriented Cu<sub>2</sub>O and oxygen vacancies synergistically promoting CO<sub>2</sub> electroreduction to formate on Cu-based hollow fiber, *J. CO<sub>2</sub> Util.* 70 (2023), 102446, <https://doi.org/10.1016/j.jcou.2023.102446>.
- [38] Y. Pang, J. Li, Z. Wang, C.-S. Tang, P.-L. Hsieh, T.-T. Zhuang, Z.-Q. Liang, C. Zou, X. Wang, P. De Luna, J.P. Edwards, Y. Xu, F. Li, C.-T. Dinh, M. Zhong, Y. Lou, D. Wu, L.-J. Chen, E.H. Sargent, D. Sinton, Efficient electrocatalytic conversion of carbon monoxide to propanol using fragmented copper, *Nat. Catal.* 2 (2019) 251–258, <https://doi.org/10.1038/s41929-019-0225-7>.
- [39] Y. Zhao, X. Zu, R. Chen, X. Li, Y. Jiang, Z. Wang, S. Wang, Y. Wu, Y. Sun, Y. Xie, Industrial-current-density CO<sub>2</sub>-to-C<sub>2+</sub> electroreduction by anti-swelling anion-exchange ionomer-modified oxide-derived Cu nanosheets, *J. Am. Chem. Soc.* 144 (2022) 10446–10454, <https://doi.org/10.1021/jacs.2c02594>.
- [40] J. Gu, C.-S. Hsu, L. Bai, H.M. Chen, X. Hu, Atomically dispersed Fe<sub>3+</sub> sites catalyze efficient CO<sub>2</sub> electroreduction to CO, *Science* 364 (2019) 1091–1094, <https://doi.org/10.1126/science.aaw7515>.
- [41] H. Mistry, Y.-W. Choi, A. Bagger, F. Scholten, C.S. Bonifacio, I. Sinev, N.J. Divins, I. Zegkinoglou, H.S. Jeon, K. Kisslinger, E.A. Stach, J.C. Yang, J. Rossmeisl, B. Roldan Cuenya, Enhanced carbon dioxide electroreduction to carbon monoxide over defect-rich plasma-activated silver catalysts, *Angew. Chem. Int. Ed.* 56 (2017) 11394–11398, <https://doi.org/10.1002/anie.201704613>.
- [42] X. Peng, S.G. Karakalos, W.E. Mustain, Preferentially oriented Ag nanocrystals with extremely high activity and faradaic efficiency for CO<sub>2</sub> electrochemical reduction to CO, *ACS Appl. Mater. Interfaces* 10 (2018) 1734–1742, <https://doi.org/10.1021/acsami.7b16164>.
- [43] M. Ma, K. Liu, J. Shen, R. Kas, W.A. Smith, In situ fabrication and reactivation of highly selective and stable Ag catalysts for electrochemical CO<sub>2</sub> conversion, *Acs Energy Lett.* 3 (2018) 1301–1306, <https://doi.org/10.1021/acscenergylett.8b00472>.
- [44] G. Barati, V. Solokha, K. Wandelt, K. Hingerl, C. Cobet, Chloride-induced morphology transformations of the Cu(110) surface in dilute HCl, *Langmuir* 30 (2014) 14486–14493, <https://doi.org/10.1021/la502589k>.
- [45] M.-H. Chien, S. Vazquez-Miranda, R. Sharif, K. Hingerl, C. Cobet, In situ optical quantification of adsorbates and surface charges on copper crystals and their impact on the hydrogen evolution reaction in hydrochloric electrolytes, *J. Phys. Chem. C* 122 (2018) 8984–8997, <https://doi.org/10.1021/acs.jpcc.8b01149>.
- [46] C. Zhao, G. Luo, X. Liu, W. Zhang, Z. Li, Q. Xu, Q. Zhang, H. Wang, D. Li, F. Zhou, Y. Qu, X. Han, Z. Zhu, G. Wu, J. Wang, J. Zhu, T. Yao, Y. Li, H.J.M. Bouwmeester, Y. Wu, In situ topotactic transformation of an interstitial alloy for CO electroreduction, *Adv. Mater.* 32 (2020) 2002382, <https://doi.org/10.1002/adma.202002382>.
- [47] J. Li, A. Xu, F. Li, Z. Wang, C. Zou, C.M. Gabardo, Y. Wang, A. Ozden, Y. Xu, D.-H. Nam, Y. Lum, J. Wicks, B. Chen, Z. Wang, J. Chen, Y. Wen, T. Zhuang, M. Luo, X. Du, T.-K. Sham, B. Zhang, E.H. Sargent, D. Sinton, Enhanced multi-carbon alcohol electroproduction from CO via modulated hydrogen adsorption, *Nat. Commun.* 11 (2020) 3685, <https://doi.org/10.1038/s41467-020-17499-5>.
- [48] W. Luc, X. Fu, J. Shi, J.-J. Lv, M. Jouny, B.H. Ko, Y. Xu, Q. Tu, X. Hu, J. Wu, Q. Yue, Y. Liu, F. Jiao, Y. Kang, Two-dimensional copper nanosheets for electrochemical reduction of carbon monoxide to acetate, *Nat. Catal.* 2 (2019) 423–430, <https://doi.org/10.1038/s41929-019-0269-8>.
- [49] R.V. Singh, M.R. Pai, A.M. Banerjee, C. Nayak, S. Phapale, D. Bhattacharyya, A. K. Tripathi, Cu-Cl thermochemical water splitting cycle: probing temperature-dependent CuCl<sub>2</sub> hydrolysis and thermolysis reaction using in situ XAS, *J. Therm. Anal. Calorim.* 147 (2022) 7063–7076, <https://doi.org/10.1007/s10973-021-10969-y>.
- [50] A.S. Varela, W. Ju, T. Reier, P. Strasser, Tuning the catalytic activity and selectivity of Cu for CO<sub>2</sub> electroreduction in the presence of halides, *ACS Catal.* 6 (2016) 2136–2144, <https://doi.org/10.1021/acscatal.5b02550>.
- [51] A. Guan, Q. Wang, Y. Ji, S. Li, C. Yang, L. Qian, L. Zhang, L. Wu, G. Zheng, Steric effect induces CO electroreduction to CH<sub>4</sub> on Cu-Au alloys, *J. Mater. Chem. A* 9 (2021) 21779–21784, <https://doi.org/10.1039/d1ta06162c>.
- [52] M. Jouny, J.-J. Lv, T. Cheng, B.H. Ko, J.-J. Zhu, W.A. Goddard, F. Jiao, Formation of carbon–nitrogen bonds in carbon monoxide electrolysis, *Nat. Chem.* 11 (2019) 846–851, <https://doi.org/10.1038/s41557-019-0312-z>.